



Strong seismic anisotropy in the deep upper mantle beneath the Cascadia backarc: Constraints from probabilistic finite-frequency SKS splitting intensity tomography

Puskar Mondal*, Maureen D. Long

Department of Geology and Geophysics, Yale University, New Haven, CT, USA

ARTICLE INFO

Article history:

Received 4 November 2019
 Received in revised form 15 February 2020
 Accepted 18 February 2020
 Available online xxxx
 Editor: M. Ishii

Keywords:

seismic anisotropy
 model space search
 tomography
 finite frequency
 splitting intensity
 Cascadia

ABSTRACT

The volcanically active High Lava Plains (HLP) region is a striking tectonomagmatic feature of eastern Oregon, in the backarc of the Cascadia subduction zone. It features young (<12 Ma), bimodal volcanic activity; the rhyolitic volcanism has a spatiotemporal trend that is oblique to that expected from the absolute motion of the North American plate. Several models have been proposed to explain the tectonic evolution of Cascadia backarc and the relationships between upper mantle processes and volcanic activity; however, consensus remains elusive. Because seismic anisotropy in the upper mantle reflects processes such as mantle flow and partial melting, constraints on anisotropic structure can shed light on the connections between mantle dynamics and tectonomagmatic activity in the Cascadia backarc. Anisotropy is often constrained via SKS splitting measurements; however, their interpretation is typically ambiguous because they lack depth resolution. Here we present new constraints on upper mantle anisotropy beneath the HLP region from probabilistic finite-frequency SKS splitting intensity tomography, which provides both lateral and depth constraints on anisotropic structure. Our technique is based on a Markov chain Monte Carlo approach to searching parameter space, and we use finite-frequency sensitivity kernels to relate model perturbations to splitting intensity observations. We use data from broadband stations of the dense High Lava Plains experiment, which provide good resolution of upper mantle anisotropic structure, as demonstrated via resolution tests. We find evidence for particularly strong seismic anisotropy in the deep upper mantle (200–400 km depth) beneath the Cascadia backarc, suggesting that flow in the deep upper mantle, rather than alignment of partial melt in the shallow mantle, provides the first-order control on shear wave splitting delay times. Our model provides additional support for the idea that mantle flow beneath the Cascadia backarc is controlled by rollback subduction. Our results suggest that anisotropy in the deep upper mantle may be more important to the interpretation of SKS splitting measurements in some settings than commonly appreciated, and provides an avenue for reconciling apparently contradictory constraints on anisotropic structure from surface waves and SKS splitting.

Published by Elsevier B.V.

1. Introduction

Located in the tectonically active western United States (e.g., Humphreys and Coblenz, 2007), the High Lava Plains (HLP) of Oregon stands out as a distinctive feature of the Cascadia subduction zone backarc (Fig. 1). Notable characteristics of the HLP include bimodal volcanism over the past ~12 Ma, encompassing both age-progressive rhyolitic volcanism and basaltic volcanism that is widespread in space and time (e.g., Jordan et al., 2004; Till et al.,

2013; Ford et al., 2013). Notably, the spatiotemporal progression of the rhyolites is oblique to plate motion, and volcanism in the HLP is contemporaneous with, but in a different geometry than, the Yellowstone/Snake River Plain trend to the west (e.g., Jordan et al., 2004; Ford et al., 2013). Several hypotheses have been proposed to explain the origin and evolution of volcanic trends in the Cascadia backarc (e.g., Long et al., 2012; Camp, 2019). These include models that emphasize the effect of a deep mantle plume that impinged on the western North American lithosphere around 17 Ma (e.g., Smith et al., 2009; Camp and Ross, 2004; Camp, 2019), those that invoke the rollback, steepening, tearing, and/or fragmentation of the Juan de Fuca slab at depth (e.g., James et al., 2011; Long

* Corresponding author.

E-mail address: pushkarmondal@gmail.com (P. Mondal).

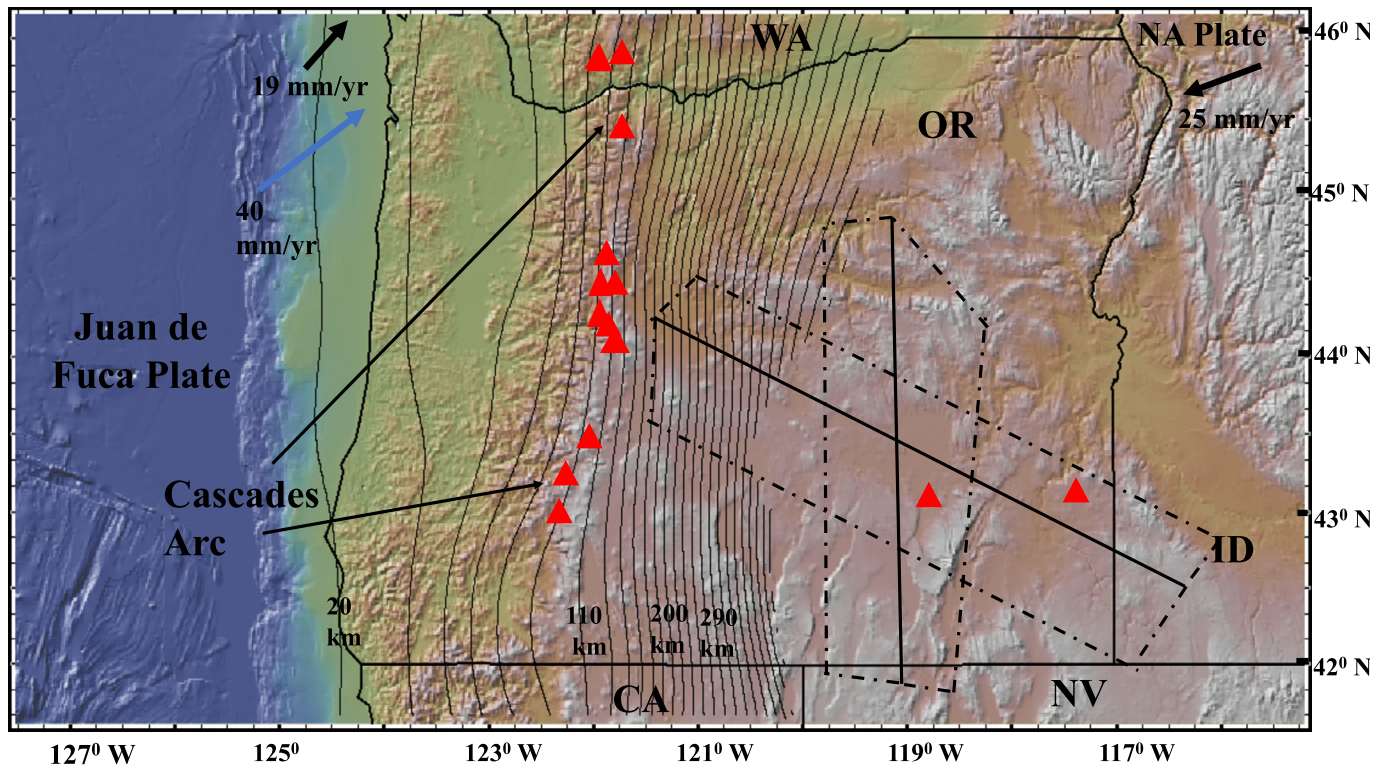


Fig. 1. General tectonic setting and geographic features of the Cascadia subduction zone. Background colors show topography (onshore) and bathymetry (offshore); Holocene volcanoes are marked with red triangles (Smithsonian Global Volcanism Program; volcano.si.edu). Thin black lines show the outlines of US states (Washington, Oregon, California, Idaho, and Nevada are marked with two-letter abbreviations). The North American (NA) and Juan de Fuca Plates are marked. Thick black arrows show absolute motion of the major plates in a hotspot reference frame, and thick blue arrow shows the relative motion (convergence direction) between the Juan de Fuca and North American plates. The vertical contours represent the depths of the Juan de Fuca plate varying between 20 and 410 km with an interval of 15 km (Slab 2.0 model, Hayes et al. (2018)). Dashed boxes represent the regions under study, with black lines representing the location of the dense lines of the HLP seismic experiment. The box oriented NW-SE roughly corresponds to the location of the High Lava Plains province. Plate motion directions and rates (shown) were calculated using the UNAVCO plate motion calculator (<https://www.unavco.org/dxdt/model>). (For interpretation of the colors in the figure(s), the reader is referred to the web version of this article.)

et al., 2012; Leonard and Liu, 2016), those that appeal to lithospheric delamination as a main driver for volcanism (e.g., Hales et al., 2005; Camp and Hanan, 2008), and those that foreground the effect of preexisting lithospheric structures (e.g., Tikoff et al., 2008). In order to discriminate among these different hypotheses, a thorough understanding of the present-day mantle flow field, and the driving forces for that flow, is necessary (e.g., Long, 2016).

Over the past decade, a wealth of geophysical observations has become available for the Cascadia backarc region, including those collected as part of the EarthScope USArray effort (including the Transportable Array, or TA) and those that resulted from the interdisciplinary High Lava Plains Project. Taken together, these data sets have yielded new insights into the structure and dynamics of the crust and upper mantle beneath the HLP, and include analyses based on SKS splitting (e.g., Xue and Allen, 2006; Long et al., 2009; Wagner and Long, 2013; Liu et al., 2014), body wave tomography (e.g., Schmandt and Humphreys, 2010; Hawley and Allen, 2019), surface wave tomography (e.g., Wagner et al., 2012, 2013; Wagner and Long, 2013), ambient noise tomography (e.g., Wagner et al., 2012), receiver function analysis (e.g., Eagar et al., 2011), and scattered wave imaging (Chen et al., 2013). One of the most striking geophysical characteristics of the HLP is the strong seismic anisotropy in the upper mantle beneath the region. Specifically, SKS splitting with delay times of up to ~ 2.5 s has been documented beneath the region (Xue and Allen, 2006; Long et al., 2009; Wagner and Long, 2013); these delay times are among the highest documented in western North America (e.g., Liu et al., 2014) or in any continental region worldwide. Evidence for relatively strong anisotropy in the upper mantle also comes from surface wave analysis (e.g., Yuan and Romanowicz, 2010; Wagner and Long, 2013).

While the particularly strong upper mantle anisotropy beneath the HLP is notable, its interpretation remains ambiguous, largely due to the path-integrated nature of SKS splitting measurements and the challenges inherent in reconciling SKS splitting and surface wave-based measures of anisotropy (e.g., Wagner and Long, 2013). Nearly vertically propagating SKS waves, when interpreted in a ray theoretical framework, have little or no depth resolution, leading to ambiguity in their physical interpretation (e.g., Long and Silver, 2009). (In some cases indirect inferences can be made based on a spatial coherency argument; e.g., Liu and Gao (2011)). Large splitting delay times, for example, may yield several different interpretations in terms of the strength and mechanism for anisotropy (i.e., a thin highly anisotropic layer vs. a thicker layer with weaker anisotropy). Similarly, in the presence of multiple layers of anisotropy with varying geometries, individual apparent fast direction measurements reflect a complicated (and non-commutative) combination of layer parameters (e.g., Silver and Savage, 1994), and isolating the depth extent of different anisotropic layers is a major challenge. In the context of the scientific questions underpinning the study of the origin and evolution of the HLP, the depth distribution of upper mantle anisotropy is a crucial question. Long et al. (2009) proposed several different scenarios that could explain the spatial variability in delay times observed beneath the HLP, variously invoking strong anisotropy in the uppermost mantle due to aligned partial melt, variations in the thickness of the anisotropic layer, or locally enhanced strength of lattice preferred orientation (LPO) in olivine. Discriminating among these scenarios is vital for our understanding of present-day mantle flow beneath the HLP region; furthermore, given that isotropic tomography models are biased in the presence of strong anisotropy

(e.g., Bezada et al., 2016), detailed knowledge of the depth distribution of anisotropy is necessary to obtain accurate images of upper mantle structure.

Substantial effort has been devoted to developing theoretical frameworks and practical strategies for inverting SKS splitting observations for anisotropic structure, much of it in the context of finite-frequency sensitivity kernels that relate model perturbations to splitting observations (e.g., Favier and Chevrot, 2003; Chevrot, 2006; Long et al., 2008; Sieminski et al., 2008; Monteiller and Chevrot, 2011; Lin et al., 2014). While these tomographic approaches have enabled progress in understanding the 3D distribution of seismic anisotropy in a few well-sampled regions, they all share a significant limitation in that the inversion strategy is based on linearization around a starting model, which may bias the model estimation. Furthermore, shear wave splitting tomography has only been applied to actual data sets in a very few regions, including subduction zones that have abundant seismicity that can be sampled with local S waves (e.g., Abt and Fischer, 2008) and regions with exceptionally dense station coverage that can be sampled with SKS waves in a finite-frequency framework (Monteiller and Chevrot, 2011; Lin et al., 2014).

Here we present an application of a model space search approach to finite frequency SKS splitting tomography, developed by Mondal and Long (2019), to the densely sampled HLP region of the Cascadia backarc. The station spacing of the broadband HLP array, which included over 100 stations, is approximately 10–15 km in its densest portions, allowing us to produce a robust model for upper mantle anisotropy beneath the HLP that is well resolved both laterally and with depth. We reprocessed data from the HLP array and USArray TA stations to obtain high-quality measurements of splitting intensity (Chevrot, 2000), which were used as input into our probabilistic inversion. The resulting models allow us to distinguish among the different scenarios proposed by Long et al. (2009).

2. Probabilistic finite frequency SKS splitting intensity tomography: methodology

We implement the model space search technique for SKS splitting intensity tomography in a finite frequency framework developed by Mondal and Long (2019). Here we briefly describe our methodology; a more detailed description of the underlying theory is contained in the online Supplementary Information, and a full explanation of the method is contained in Mondal and Long (2019). Due to the nearly vertical propagation of SKS phases, the application of finite frequency theory is necessary in SKS splitting tomography (Chevrot, 2006). In this framework, the superposition of multiple finite-frequency sensitivity kernels of adjacent stations provides a means of localizing structure. We rely on observations of the splitting intensity (Chevrot, 2000), a measure of the amount of energy on the transverse component waveform; in the absence of shear wave splitting, the SKS phase will be radially polarized. Following Chevrot (2000), shear wave splitting intensity (S) is defined as

$$S(\mathbf{r}) = 2 \frac{\text{Re} \int \omega \delta u^T(\mathbf{r}, \omega) u_0^{*R}(\mathbf{r}, \omega) d\omega}{\int \omega^2 |u_0^R(\mathbf{r}, \omega)|^2 d\omega}, \quad (1)$$

where δu^T , u_0^R , ω , and \mathbf{r} are the transverse and radial component of the displacement, angular frequency, and station locations, respectively.

Our parameterization of anisotropy uses insights from experimental and observational constraints on lattice preferred orientation (LPO) in olivine aggregates, thought to be primarily responsible for seismic anisotropy in the upper mantle (Karato et al., 2008). We assume that olivine aggregates can be represented as

a linear mixture of two endmembers: an isotropic equivalent, in which the individual grains are randomly oriented, and a perfectly aligned aggregate, in which the elasticity is equivalent to a single crystal of olivine. In this scheme, the strength of anisotropy can be represented with a parameter (χ) that varies from 0 (random alignment) to 1 (complete alignment). We further assume that the elasticity of the perfectly aligned olivine endmember can be well described by a hexagonal approximation.

Using this parameterization, we established the following relation between the splitting intensity and the anisotropy parameters (Mondal and Long, 2019):

$$S(\mathbf{r}) = \int_{\Omega} K_{\chi}(\mathbf{r}, \theta, \phi; \mathbf{r}') \chi(\mathbf{r}') d^3 \mathbf{r}', \quad (2)$$

where K_{χ} is the corresponding sensitivity kernel, which is itself a non-linear function of the orientation parameters (θ, ϕ). Here, θ and ϕ represent the dip and the azimuth of the symmetry axis of the anisotropy. We do not require sensitivity kernels for the orientation parameters θ and ϕ as we do not perform a linearized inversion. Instead, the sensitivity kernel for the strength parameter depends on θ and ϕ and therefore, with each iteration the sensitivity kernel is updated as one moves through parameter space. Examples of sensitivity kernels are shown in Fig. 2. There is a strong non-linear relationship between the splitting intensity and the anisotropy parameters (θ, ϕ). Rather than constructing a linearized inversion, then, our inversion strategy invokes a Markov chain Monte Carlo search technique based on the adaptive Gibbs sampling algorithm. Such a technique satisfies the requirement that the outcome does not depend on the starting model, as the model space is sampled randomly following the particular probability distribution. In order to represent the most likely model from our probability distributions, we rely on an ensemble average (Ruelle, 1999) which is suitable for multimodal distributions.

3. Data and measurements

The High Lava Plains project and the EarthScope USArray Transportable Array (TA) provide a wealth of broadband seismic data in and around the HLP region. Between the HLP and TA deployments, there are 137 densely distributed broadband stations in the region, operated between 2006 and 2009. The HLP station configuration consists of two dense lines surrounded by a “cloud” of stations (Fig. 3). The first line spans from southwest Idaho to northwest Oregon, ending just to the west of the Cascades Range. This line follows the time-progressive track in rhyolitic volcanism (e.g. Ford et al., 2013). The second dense line is aligned almost N-S from Basin and Range extension (south) through HLP volcanism to the accreted terranes of Oregon’s Blue Mountains (Fig. 3a). The average spacing between each station along the dense lines is approximately 10 – 15 km, appropriate for our analysis.

Shear wave splitting measurements are a routine procedure in the study of seismic anisotropy. SKS splitting parameters (fast directions and delay times) for stations of the HLP experiment and nearby TA stations have been measured previously by Long et al. (2009) and Wagner and Long (2013). In our analysis we require measurements of splitting intensity, a scalar entity obtained by computing zero-lag cross-correlation between the transverse component and the time differentiated radial component of the seismogram. Therefore, we reprocessed the HLP and TA datasets using the Split-Racer software, recently developed by Reiss and Rumpker (2017). Split-Racer estimates splitting intensity and associated errors and allows rapid processing of a large number of waveforms.

We processed and measured approximately 2000 waveforms with high quality SKS phases. We selected events of magnitude $M_w \geq 6$ located at epicentral distances between 90° and 130°. An

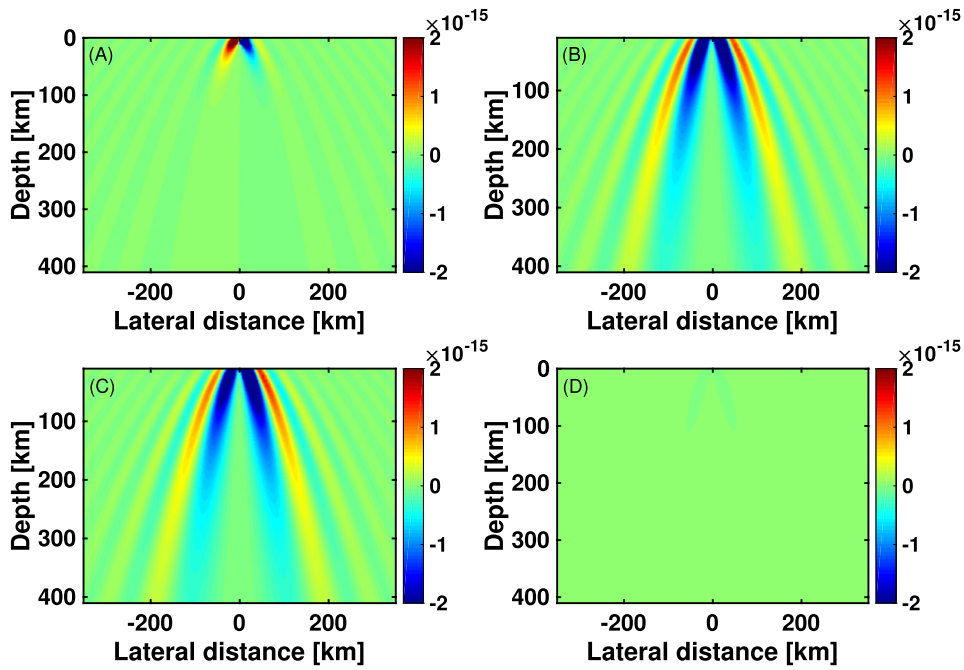


Fig. 2. Sensitivity kernel examples showing a 2-D slice along the plane of wave propagation. Plots show the behavior of the sensitivity kernels for the anisotropy strength at different values of the azimuth of the symmetry axis (ϕ) while the dip of the symmetry axis ($\theta = 0^\circ$), and the incoming polarization direction ($\alpha = 0^\circ$) remain fixed. (A) Symmetry axis is parallel to the polarization direction ($\phi = 0^\circ$): the kernel is perfectly antisymmetric, leading to a zero splitting intensity for a homogeneous anisotropic model. (B) $\phi = 30^\circ$, (C) $\phi = 60^\circ$. For these examples the kernels are symmetric. (D) Symmetry axis is perpendicular to the polarization direction ($\phi = 90^\circ$): the sensitivity kernel is trivially zero, yielding zero splitting intensity for arbitrary spatial distribution of anisotropic strength. Unit of the sensitivity is m^{-2}s . The frequency range associated with the computation of these kernels is 0.04-0.125 Hz.

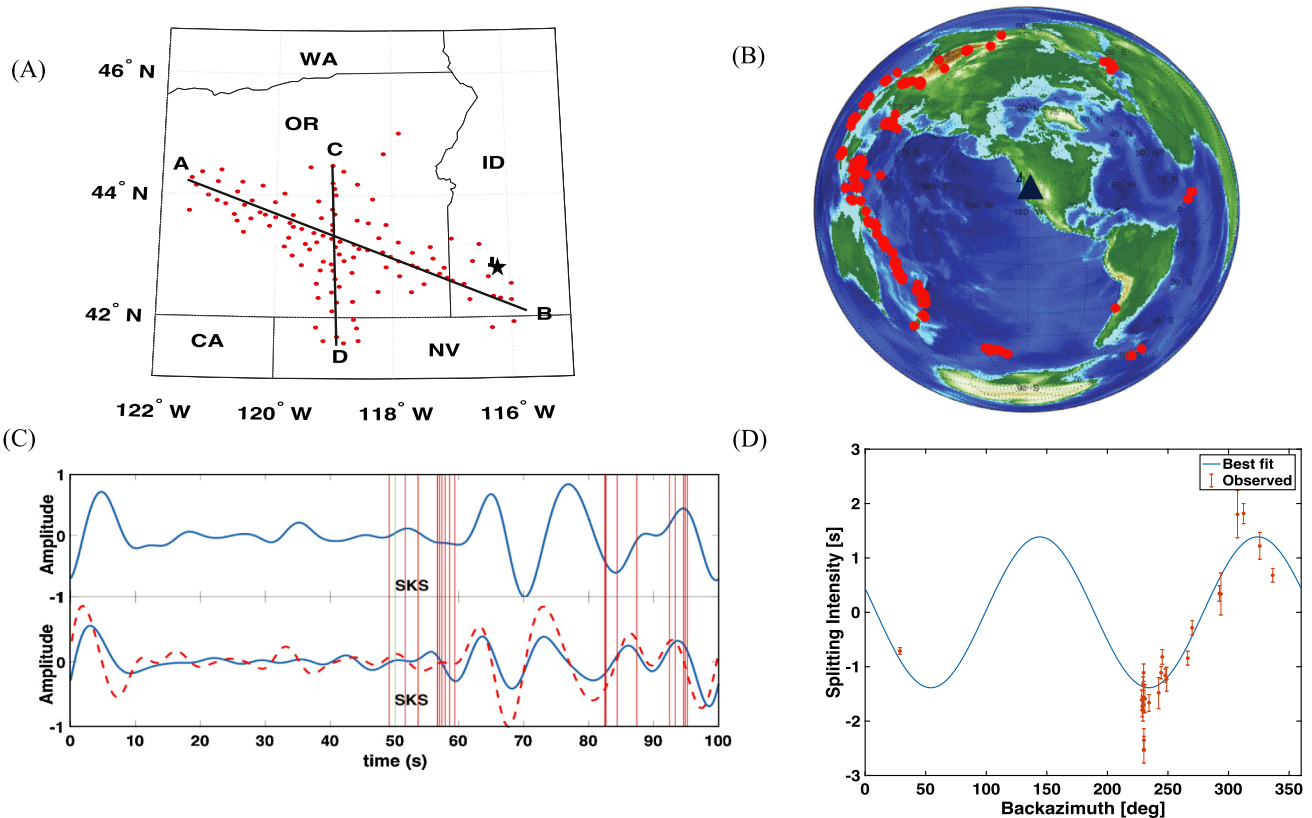


Fig. 3. (A) The station distribution used in this study, shown by the red dots. The two dense arrays are marked as AB and CD. The star indicates the location of station ID005, shown in panel D. (B) Map of events used. (C) An example of the SKS split phase (in the red time window) observed at the station ID005. The blue trace in the top panel represents the radial component of the SKS waveform while the blue trace in the bottom panel shows the transverse component. The red dotted line is the time derivative of the radial component. The red lines indicate a selection of the multiple time windows automatically chosen by the splitting algorithm, as described by Reiss and Rümpler (2017). (D) The splitting intensity data plotted as a function of the backazimuth of the events observed at station ID005. The red bars denote the observed measurements while the blue line is the best fit of a $\sin(2\theta)$ curve to this observed data. Black star on (A) indicates the position of the station ID005.

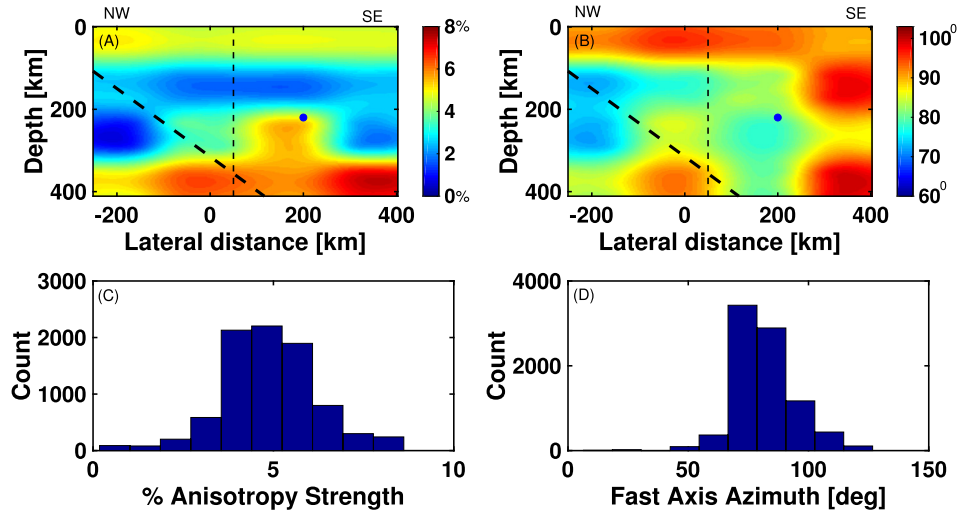


Fig. 4. Most likely model for the NW-SE line (labeled AB on Fig. 2). The spatial domain vertical section is discretized by $50 \text{ km} \times 50 \text{ km}$ grids. The image is obtained after smoothing the original $50 \times 50 \text{ km}^2$ discretized model for visual presentation. (A) Spatial distribution of the anisotropy strength, showing strong anisotropy in the deep upper mantle. Considerable spatial variation is observed, with anisotropy values ranging from 1% to 7%. (B) The spatial distribution of the fast axis azimuth, which shows only limited variation. The vertical dashed line shows the intersection of the arrays AB and CD (see Fig. 2). The inclined dashed line shows the intersection of the subducting Juan de Fuca slab with the vertical section passing through NW-SE line, from the Slab 2 model of Hayes et al. (2018). (C) Histogram showing the posterior distribution of anisotropy strength, corresponding to a well-resolved grid node marked by the dot on (A). (D) Histogram showing the posterior distribution of fast axis orientation corresponding to well-resolved grid node marked by the dot on (B).

event map is shown in Fig. 3. Each station has recorded approximately 20 high quality events on average during the specified time interval. We applied a bandpass filter to retain energy at periods between 8 and 25 s, and visually examined the horizontal components of the SKS waveform to retain waveforms with a high signal to noise ratio ($\text{SNR} > 2.5$) and with a transverse component that takes the shape of the time derivative of the vertical component. After the quality checks, we obtained 1292 robust SKS splitting intensity measurements which were found to be exceptionally high quality. Examples of an SKS splitting intensity measurement and the splitting intensity curve for station ID005 are presented in Fig. 3. Additional examples of splitting intensity curves for HLP stations are shown in Supplementary Fig. S1.

4. Results

Here we present the results from our two 2-D inversions along the dense lines of the HLP experiment (Fig. 3). These two inversions were carried out separately; given the computational limitations of a model space search approach, a 2-D inversion approach is tractable (Mondal and Long, 2019). A check of the consistency between the two models at the intersection point is discussed in section 4.3, which also presents a pseudo-3D model for the region based on the 2-D inversions. We restrict our attention to the inversion of the strength parameter (χ) and the azimuth of the fast axis (ϕ); we assume that the symmetry axis is horizontal. Providing a reasonable constraint on the dip (θ) of the fast axis is unlikely due to the fact that the SKS wave propagation direction is nearly vertical, as discussed in Mondal and Long (2019). In addition, we restrict the anisotropy strength to be less than 10%, a reasonable upper limit for most of the upper mantle.

4.1. Anisotropy model of the NW-SE array

Striking lateral variations in SKS splitting delay times were measured along the NW-SE trending dense line of the HLP experiment, along with more modest variations in measured fast directions. The highest delay times (up to ~ 2.5 s) are roughly in the central portion of the transect (Wagner and Long, 2013; see their Fig. 6). This variability suggests variation in the strength of

anisotropy beneath the HLP, laterally and/or with depth, but previous investigations have left the depth range of this variability ambiguous.

Our preferred inversion was carried out with a cell size of $50 \text{ km} \times 50 \text{ km}$, based on previous work (Mondal and Long, 2019) and on resolution considerations that are discussed in Section 5. A total of 822 splitting measurements from 63 stations were used as the input for our inversion and convergence was attained after approximately 140,000 iterations (a total of 256,000 iterations were performed). While we solve for anisotropy parameters throughout the model domain, down to a depth of 400 km, our focus is on the depth range between 50–400 km, as resolution tests show that the shallow portion of our model is not well resolved. Because our tomographic approach is probabilistic, we obtain posterior probability distributions for each parameter for each grid point, rather than a single estimate. We present our models by plotting the most likely parameter values (that is, the values that were most heavily sampled by the Markov chain, as expressed by the value of the ensemble average), along with histograms showing the probability distributions for selected portions of the model. A full set of histograms for regions throughout the model space are shown in Supplementary Figs. S2-S3; similar figures for the N-S model (discussed in section 4.2) are shown in Supplementary Figs. S4-S5.

Our model for the NW-SE dense line, shown in Fig. 4, reveals intriguing variations in both the strength of anisotropy (plotted as % anisotropy in Fig. 4a) and, to a lesser extent, the fast direction orientation (plotted as azimuth from N in Fig. 4b). Anisotropy strength ranges from relatively weak values (~ 1 –2%) up to a maximum of $\sim 8\%$, while fast directions exhibit comparatively weak variability (values ranging from $\sim 60^\circ$ to 105° east of north). The model features include anisotropy that is relatively uniform with a strength of ~ 4 –5% and a fast direction that is close to E-W in the uppermost mantle (depths between 50–100 km). Between 100–200 km depth, anisotropy is surprisingly weak, with values of $\sim 2\%$, and fast orientations that range from $\sim 70^\circ$ in the NW to $\sim 95^\circ$ in the SE. Below 200 km, there is considerably stronger anisotropy, with values of ~ 6 –8% in the 300–400 km depth range. For the most part, the region of strong anisotropy in the deep upper mantle lies above the slab surface (Fig. 4a). In the 200–300 km depth

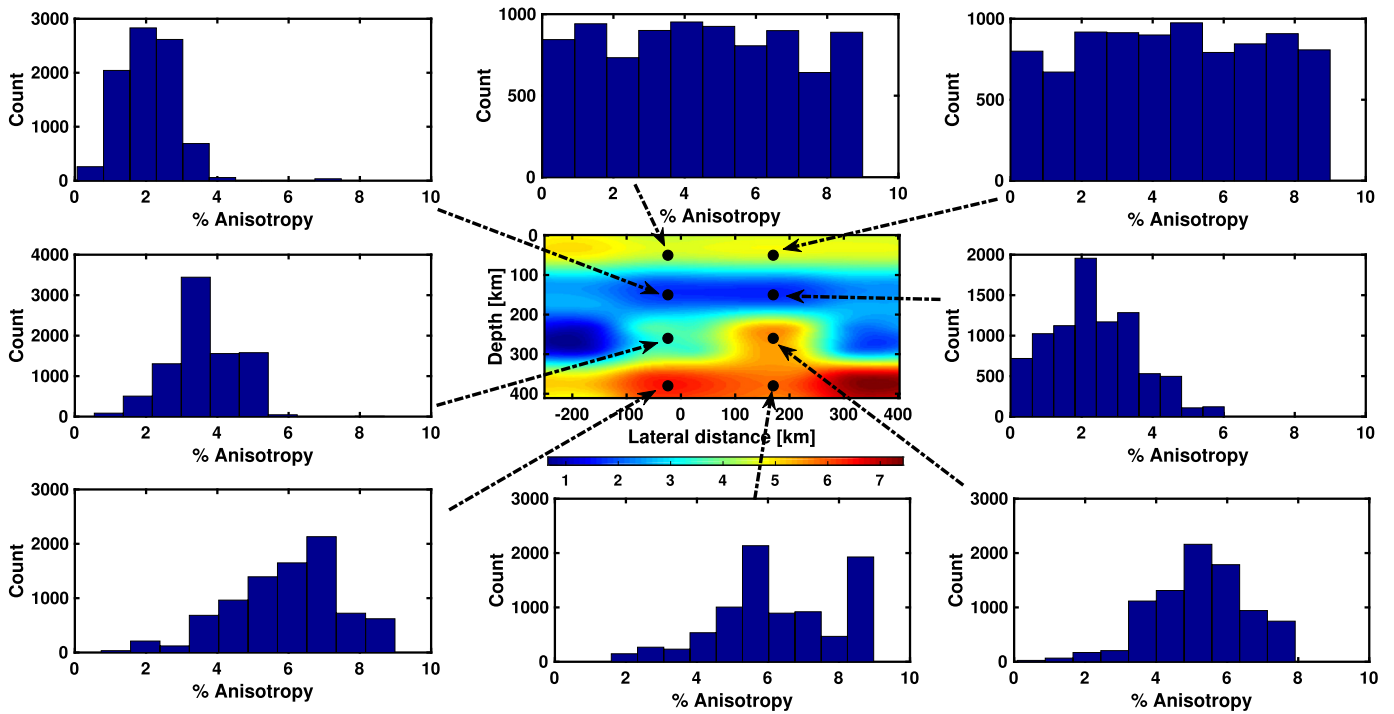


Fig. 5. Posterior distributions of the most likely recovered model for anisotropy strength along the NW-SE line, shown in Fig. 4a. These demonstrate that the shallow part of the model (<50 km) is poorly constrained, whereas the deeper parts, with considerable overlapping of the sensitivity kernels, yield a fairly good resolution.

range, there is notable variation in both fast directions and delay times, with a region in the central portion of the array that exhibits stronger anisotropy, and a counterclockwise rotation in fast axis orientation, compared to the adjacent regions.

While Fig. 4 shows the most likely model for anisotropy beneath the NW-SE line, it is crucial to understand the character of the probability distributions for anisotropy parameters in order to appreciate how well constrained different portions of the model are. We have examined these distributions for our entire model space (Supplementary Figs. S2-S3), and illustrate selected histograms for the anisotropy strength parameter in Fig. 5. As expected, our model is poorly resolved in the shallowest part (above 50 km); in this depth range we do not achieve overlapping sensitivity kernels with the station density available, and we therefore do not interpret this portion of the model. Elsewhere, the histograms reveal that the distributions are much tighter, and parameters are much better constrained. In particular, both in the depth range associated with weak anisotropy (100-200 km) and in the deeper portions with strikingly strong anisotropy (300-400 km), the histograms of model parameters show that they are generally tightly constrained by the observations.

4.2. Anisotropy model of the N-S array

A total of 470 splitting measurements from 47 stations were used as the input for our inversion beneath the N-S line (corresponding to the line CD in Fig. 3a) and convergence is attained after approximately 140,000 iterations (a total of 256,000 iterations were performed). As with the NW-SE line, we used a grid spacing of 50 km \times 50 km. Again as with the NW-SE line, this line cuts across the region of particularly large splitting delay times identified by Long et al. (2009) and Wagner and Long (2013), so we expect to see lateral and/or depth variations in anisotropy strength in our model. This expectation is borne out by the model in Fig. 6, which exhibits strong anisotropy in the deep upper mantle (200-400 km depth range) in the central portion of the model, with weaker anisotropy in this depth range at the edges. Furthermore,

in the asthenospheric upper mantle (depth range 100-200 km), there are dramatic lateral variations in anisotropy strength. We document a region of strong anisotropy located just to the south of the crossing point between the NW-SE and N-S dense lines. Interestingly, this region of locally strong anisotropy ($\sim 7\%$) is juxtaposed with a region of much weaker anisotropy ($\sim 2\%$) in the same depth range just to the north. The strong anisotropy in the 100-200 km depth range coincides geographically with a region of particularly high delay times documented by Long et al. (2009), suggesting that constructive interference between anisotropy layers at different depths may contribute to the particularly large δt observed in the central portion of the HLP.

Our model for the spatial variability in fast axis orientations shows more consistent layering than the corresponding model for the NW-SE line (Fig. 4b), but as with the NW-SE model, the actual variability in orientations is relatively minor. We see fast directions that are nearly E-W in the shallower portions of the model (depths shallower than 200 km). In the deeper portions of the model, the most likely fast axis orientations are rotated slightly counterclockwise from the shallower portions ($\sim 70^\circ$ - 80° east of north); however, the difference is slight, and is likely not dramatic enough to cause strong variability in apparent splitting parameters with backazimuth at most azimuthal ranges (Silver and Savage, 1994). This is consistent with the observation that apparent splitting parameters generally do not vary with backazimuth at HLP stations (e.g., Wagner and Long, 2013; see their Fig. 2).

4.3. Consistency checks and a pseudo-3D model

Because we have carried out two separate 2D inversions, a natural check on our results is to compare the variation in anisotropy parameters with depth at the point at which the two models cross. Of course, the two models are not completely independent, in the sense that a portion of the splitting intensity observations were included in both inversions; specifically, data from 13 stations, representing a total of 119 measurements, were used in both inversions. Still, a consistency check between the two independent

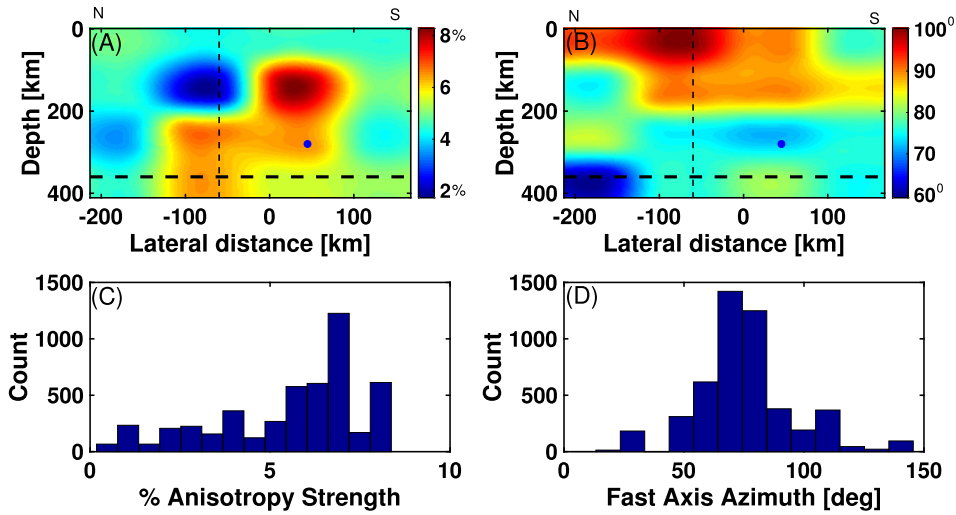


Fig. 6. Most likely model for the N-S line (labeled CD on Fig. 2). The spatial domain vertical section is discretized by 50 km × 50 km grids. The image is obtained after smoothing the original 50 × 50 km² discretized model for visual presentation. (A) Spatial distribution of the anisotropy strength showing strong anisotropy in the deep upper mantle, as well as a localized strong shallow (100-200 km) anisotropy feature, between 0 and 100 km. Considerable spatial variation is observed, with anisotropy values ranging from 1% to 7%. (B) The spatial distribution of the fast axis azimuth, which shows only limited variation. The horizontal dashed line shows the intersection of the subducting Juan de Fuca slab with the vertical section passing through N-S line, from the Slab 2 model of Hayes et al. (2018). The vertical dashed line shows the intersection of the arrays AB and CD (see Fig. 3). (C) Histogram showing the posterior distribution of anisotropy strength, corresponding to a well-resolved grid node marked by the dot on (A). (D) Histogram showing the posterior distribution of fast axis orientation corresponding to well-resolved grid node marked by the dot on (B).

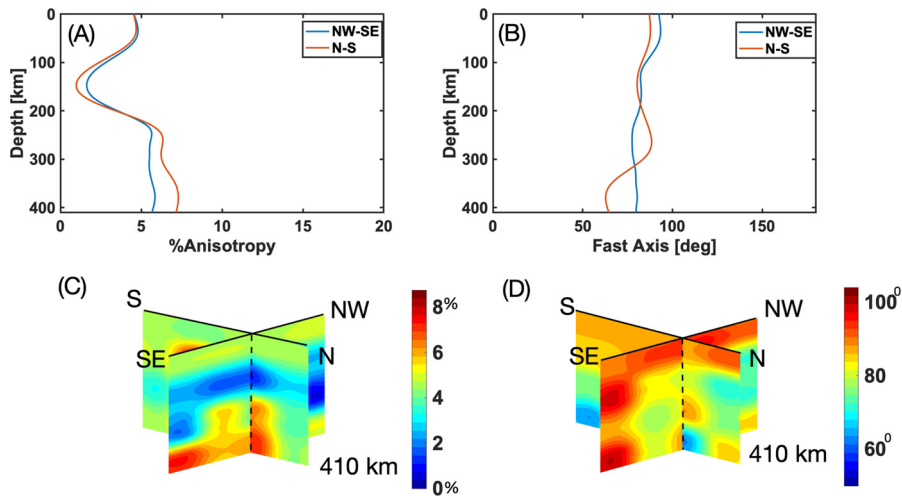


Fig. 7. Comparison of the (A) strength of anisotropy and the (B) fast axis orientation between the results obtained from two different 2D inversions (corresponding to the NW-SE (blue curves) and N-S (red curves) arrays) at the intersection point. Panels (C) and (D) show a pseudo 3-D representation of the (C) strength and (D) orientation parameter, with the orientations of each line shown.

inversions is useful; while we do not expect the most likely models at the crossing point to be identical, we do expect them to be generally consistent. As Fig. 7 shows, this expectation is borne out, particularly for the anisotropy strength parameter, which shows an excellent match for both models. The models for fast axis orientation are not quite as consistent, but they do show generally similar behavior, with orientations near 80°-90° in the shallow upper mantle and a slight counterclockwise rotation in the deep upper mantle. At depths below 200 km, the two models diverge somewhat, with differences in the most likely fast axis orientation of up to 20°.

Another way to visualize our tomography results is through the construction of a pseudo-3D model, which merges the two 2D models in the appropriate geographic reference frame (Fig. 7). This view of our most likely models again demonstrates the major features of our images, particularly the pervasive strong anisotropy in the deep upper mantle and the relatively weak anisotropy at shallower depths (100-200 km), with the exception of a region in the

southern portion of the N-S line. This view also illustrates the generally good match between the models at their intersection point.

Finally, we visualize our most likely models in map view using a series of stick diagrams (Fig. 8), which employ a common convention for representing anisotropy, with bars whose orientations correspond to the fast axis orientation and whose lengths correspond to the strength of anisotropy. We show the variation in anisotropy parameters for depth slices at 100 km, 200 km, 300 km, and 400 km. These maps again demonstrate the significant variation in strength of anisotropy with depth, with the deep upper mantle (300 km and 400 km depth slices) generally exhibiting considerably stronger anisotropy than the shallower upper mantle. The region of strong anisotropy in the central and southern portion of the study area at relatively shallow depths (100 km and 200 km depth slices) is particularly prominent. The fast axis orientations, in contrast, do not vary dramatically across our study region, either laterally or with depth. This is consistent with previous suggestions that the mantle flow field beneath the Cascadia

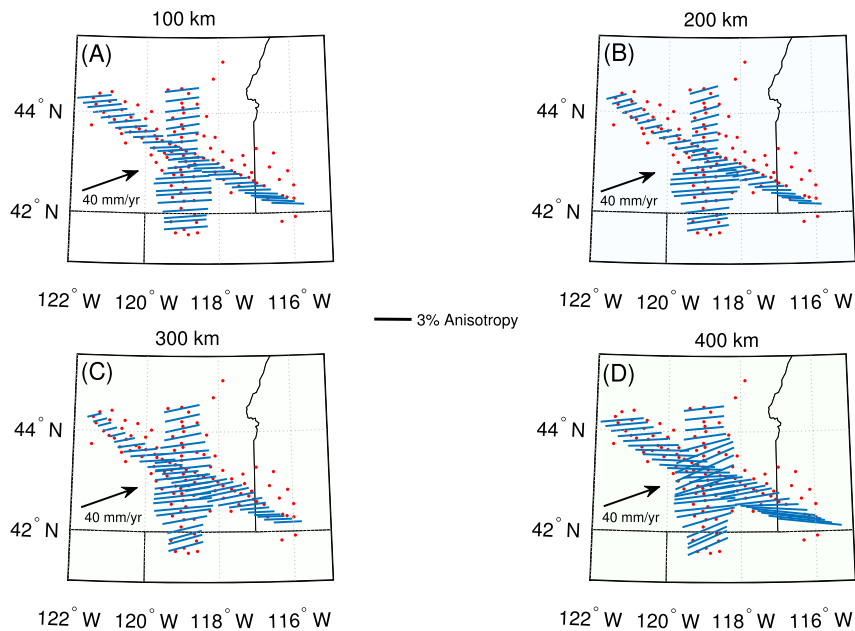


Fig. 8. Diagram of the anisotropy strength and fast axis orientation (from our most likely models) in map view along the two dense lines at different depths. The length of the bar is scaled to anisotropy strength, while the orientation of each bar shows the local orientation of fast axis. (A) At depth 100 km: the models exhibit generally relatively weak anisotropy (less than 2%) beneath most of the study region, although there is a region of locally stronger anisotropy just to the south of the crossing point between the two lines. (B) At depth 200 km: models exhibit relatively weak anisotropy $\sim 2\%$, again with generally uniform fast axis orientation. An exception is the region of notably strong anisotropy (up to 6%) just to the south of the crossing point of the two lines. (C) At depth 300 km: models exhibit stronger anisotropy with maximum anisotropy reaching up to 5%. The fast axis orientation along the NW-SE array varies from 70° in the NW to $\sim 90^\circ$ in the SE, while it remains almost uniform along the N-S line. (D) At depth 400 km: Both models exhibit strong anisotropy throughout, up to 7%. The fast axis orientation along the NW-SE line changes from $\sim 80^\circ$ in the NW to $\sim 95^\circ$ in the SE. It also varies somewhat along the N-S line, from 65° in the south to $\sim 90^\circ$ in the north. Thick black arrow shows the relative motion (convergence direction) between the Juan de Fuca and North American plates.

backarc is generally simple, and may be controlled by the rollback of the Cascadia slab (e.g., Druken et al., 2011; Long et al., 2012; Long, 2016).

5. Resolution tests

As with any tomographic inversion, the question of resolution is paramount in the interpretation of the results. Given the challenges inherent in resolving anisotropy in tomographic inversions, particularly for nearly vertically propagating SKS phases (e.g., Chevrot, 2006; Long et al., 2008), it is important to evaluate how well our anisotropy models are resolved, and to restrict our interpretations to robust features that are well-resolved and required by the observations. A series of resolution tests for synthetic data sets was presented in Mondal and Long (2019); many of these tests were aimed at highly simplified scenarios, but a subset of them used the actual HLP experiment station configuration as an example of a plausible real-world data set. These previous tests demonstrated that the HLP station configuration should allow for the resolution of anisotropic structure on length scales of ~ 50 km in most portions of the model, although there is little or no resolution of structure shallower than ~ 50 km depth. Here we build on the tests presented in Mondal and Long (2019), using the actual distribution of stations and events represented in our splitting intensity data set (rather than a synthetic, random distribution of earthquakes over all azimuths). We use our input model to create a synthetic data set of splitting intensity “observations” by computing sensitivity kernels for each event-station pair in our real data set, as described in section 2, and integrating those kernels over the model volume, according to equation (2).

We first perform a checkerboard test, shown in Fig. 9, with input anomalies that are 100 km square. Additional histograms showing probability distributions throughout the model space for this test are shown in Fig. S6. Because our preferred models themselves tend to exhibit variations on a spatial length scale of about

100 km (Figs. 4 and 6), this is a reasonable choice for an input pattern. Because most of the variability in our recovered models is in anisotropy strength, with little variability in the fast axis orientation, in this test we hold ϕ fixed at a reasonable average value of 80° . We calculate synthetic splitting intensity values for the input pattern and then use these values in the inversion scheme. The results of this test reveal several interesting properties of our inversion scheme. First, as expected, we observe significant smearing in the shallowest part of the model (depth < 50 km), and the posterior distributions for these grid nodes are spread widely throughout parameter space. This is due to the lack of substantial overlap among the sensitivity kernels at shallow depths, and is limited by the station spacing in the experiment. At depths greater than 50 km, however, the resolution test successfully recovers each of the grids of the input pattern with sufficient accuracy. As in any tomographic inversion, there is some smearing of structure, and the posterior distributions do show some spread in their values. Nevertheless, this test demonstrates that our inversion scheme is capable of resolving anisotropic structure at depth, even using only (nearly) vertically propagating SKS waves.

In the second test, shown in Fig. 10, we carry out a recovery test, in which we use the most likely model from our actual inversion (in this case, beneath the NW-SE line) as an input pattern. We calculate synthetic splitting intensity values for this most likely model, and invert those synthetic data using the same grid parameterization (50×50 km) as in the actual inversion. The results of this test show that the output model strongly resembles the input model in its first-order characteristics, although there are some differences in the detail. The synthetic inversion successfully reproduces the major features, including the relatively weak anisotropy in the 100–200 km depth range, and the particularly strong anisotropy in the deep upper mantle (particularly in the SE portion of the model). Moreover, histograms that show the poste-

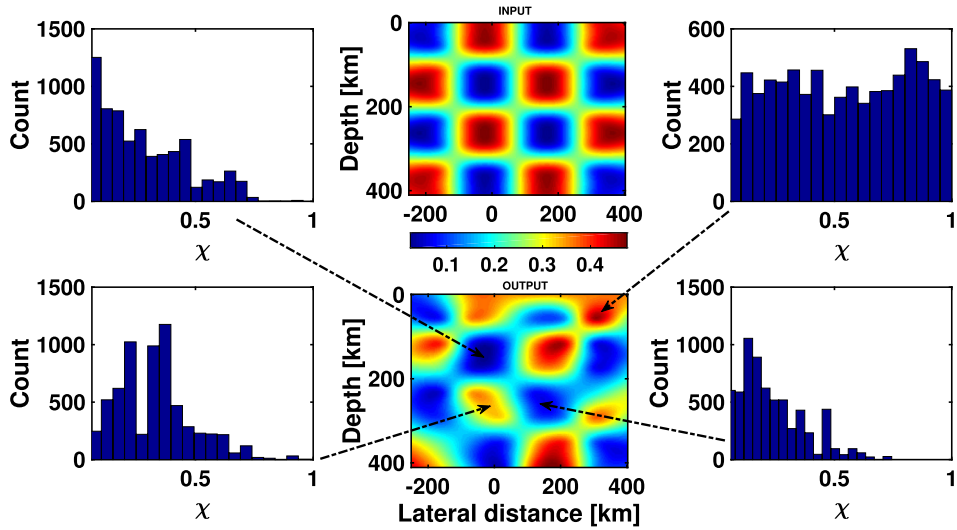


Fig. 9. Results of checkerboard resolution test. Input model is shown in the top central panel, while the bottom central panel shows the most likely recovered model, and the histograms show posterior distributions of the recovered strength of anisotropy at selected points in the model. The input pattern corresponds to a $100 \times 100 \text{ km}^2$ checkerboard of alternating strong and weak anisotropy in a model domain of $600 \times 400 \text{ km}^2$ with 50 km grid spacing. We only solve for strength χ ; the other parameters are held fixed with $\theta = 0$ and $\phi = 80^\circ$. This test demonstrates that the input is well resolved in portions of the model domain where the sensitivity kernels overlap. As expected, the shallow part of the model lacks such overlap and remains unresolved. Note that here we show values of the strength parameter χ , which takes values between 0 and 1, instead of % anisotropy.

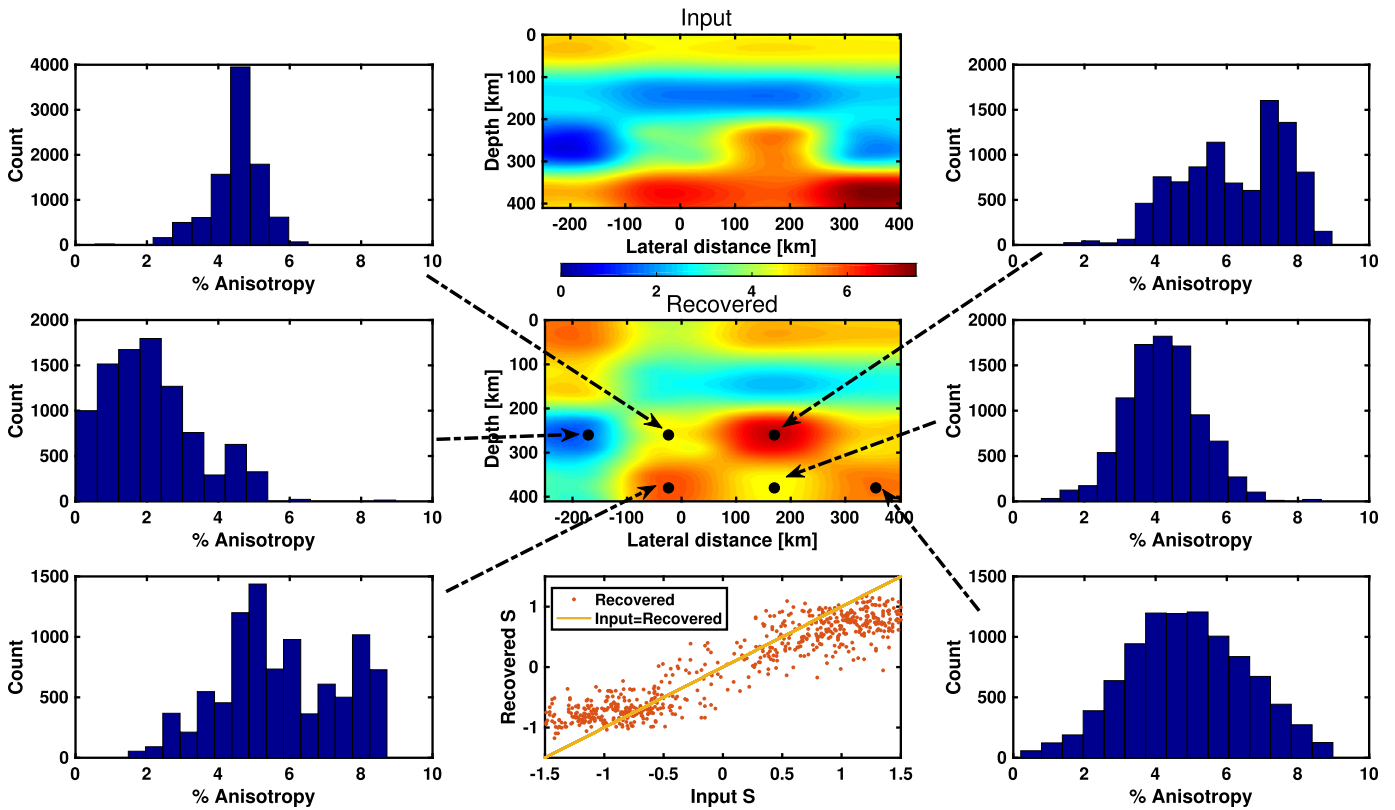


Fig. 10. Results of the recovery resolution test. Top middle panel shows the input model (the most likely model achieved from the inversion along the NW-SE line) for anisotropy strength (in %, represented by the color bar). The central panel shows the most likely recovered model. Bottom middle panel shows the correspondence between input (the synthetic splitting intensity values calculated for the input model) and output (splitting intensity values predicted for the most likely output model) splitting intensities. In general, the recovered model reproduced the input splitting intensity values well. Other panels show posterior distributions of the recovered anisotropy strength at selected points of the model (indicated by arrows), plotted as histograms.

rior probability distributions for selected grid points (Fig. 10) show that these major features are generally well resolved.

Because SKS kernels have their maximum sensitivity in the depth range extending down to roughly 300 km (Fig. 2), the question of how well our observations constrain structure in the deep-

est portions of the model is particularly crucial. As shown by the resolution tests in Figs. 9 and 10 and Supplementary Fig. S6, the inversion does retrieve structure in the $300\text{--}400 \text{ km}$ depth range, although the amplitude is imperfectly estimated. We note that there are some tradeoffs in our inversion between anisotropy in

the shallowest part of the model (shallower than 50 km, where we effectively have no resolution) and anisotropy in the deepest part of the model. One question, then, is whether the strong anisotropy that we image in the deepest parts of the model might actually reside in the shallowest part of the model, where we have poor resolution. We argue that this scenario is highly unlikely, because surface wave phase velocity maps at the periods that have maximum sensitivity in this shallow depth range do not show strong azimuthal anisotropy (Wagner and Long, 2013). This argument, together with the resolution tests presented here, give us confidence that the first-order features of our most likely models for anisotropy strength beneath the HLP - namely, the strong anisotropy in the deep upper mantle, the relatively weak anisotropy between 100-200 km depth beneath the NW-SE line, and the locally strong anisotropy anomaly between 100-200 km depth beneath the southern portion of the N-S line - are in fact required by the data and well-resolved by the inversion, and can be interpreted in terms of physical processes.

6. Discussion

6.1. Probabilistic finite-frequency SKS splitting intensity tomography: proof of concept

We have presented a first practical application of probabilistic finite-frequency splitting intensity tomography to the Cascadia backarc region. This densely distributed seismic network yields a generally robust model for upper mantle anisotropy at depths between 50-400 km. The resolution tests (Figs. 9 and 10) show that SKS splitting intensity data collected during a temporary broadband deployment are capable of constraining depth-dependent anisotropy in the upper mantle. This provides an exciting new avenue for the interpretation of SKS splitting datasets, and builds on the few previous studies that have applied finite-frequency SKS splitting tomography approaches to actual data (Monteiller and Chevrot, 2011; Lin et al., 2014)

One caveat to the successful application of probabilistic finite-frequency SKS splitting intensity tomography presented here is that the HLP splitting data set is one that displays significant variability in observed splitting delay times, but much less in observed fast splitting directions (Long et al., 2009; Wagner and Long, 2013). This makes this set of observations an easier target for our tomographic approach, since the tomography problem for anisotropy strength (for the case in which the anisotropy geometry varies little) is more nearly linear than the corresponding problem in which both the strength and geometry of anisotropy varies widely. Work to apply our analysis approach to datasets for which we expect both the geometry and strength of anisotropy to vary substantially is ongoing.

6.2. Tectonic implications

A key finding from this work is that SKS splitting intensity observations beneath the HLP prefer models that include strong anisotropy (up to ~6-8%) in the deep upper mantle (200-400 km depth range) beneath much of the Cascadia backarc. This finding contradicts the simplest expectations that might be formed from visual inspection of the traditionally measured SKS splitting parameters, as discussed in Long et al. (2009). Variations in shear wave splitting behavior over short length scales are often interpreted to require variations in anisotropy at shallow depths, based on an argument that invokes overlapping Fresnel zones (e.g., Liu and Gao, 2011). However, our work shows that the generally smooth variations in measured δt across the HLP stations (e.g., Fig. 6 in Wagner and Long, 2013) can result from the integrated effects of anisotropic layers with different strengths, including (in

this case) a layer of strong anisotropy in the deep upper mantle. Specifically, the particularly large delay times beneath the central part of the HLP study area result from the combined effect of strong anisotropy in the deep upper mantle and a localized region of strong anisotropy in the 100-200 km depth range evident in the N-S model (Fig. 6).

This finding has implications for discriminating among the different scenarios proposed as possible explanations for the large SKS splitting delay times beneath the HLP. Long et al. (2009) discussed three possible explanations for the δt values (and their spatial variability): a particularly thick anisotropic layer(s) beneath the region, particularly strong olivine LPO (perhaps due to specific deformation conditions in terms of temperature or water content), or a contribution from shape preferred orientation of partial melt in the uppermost mantle. Based on the models presented in this paper, the last of these three possibilities can be effectively ruled out: there is no evidence in our models for strong anisotropy in the shallow depth ranges at which partial melt may be present, and instead our inversions prefer models that include strong anisotropy in the deep upper mantle. While the large delay times beneath the HLP do likely reflect the constructive interference of multiple layers of anisotropy over several depth ranges, our finding that strong (~6–8% anisotropy) is required in much of the deep upper mantle, and in a localized region of the asthenospheric upper mantle along the N-S line, is consistent with the earlier suggestion by Long et al. (2009) that particularly strong olivine LPO may be present. What is surprising, however, is the extent to which this strong LPO is forming in the deep upper mantle.

What do our models imply for our understanding of the tectonic evolution of the HLP and the Cascadia backarc more generally? First, our finding of generally E-W fast axis orientations, with little variability in the geometry of anisotropy, is consistent with previous suggestions that the flow field beneath the Cascadia backarc is generally simple, and likely controlled by rollback subduction of the Juan de Fuca slab (e.g., Druken et al., 2011; Long et al., 2012; Long, 2016), perhaps in combination with other factors (e.g., Zhou et al., 2018). A comparison between our anisotropy models and isotropic velocity models for the same region derived from tomography (Schmandt and Humphreys, 2010) does not demonstrate any striking correlations between anisotropy strength and shear wave velocity (Supplementary Fig. S7), as might be expected if the strength of olivine LPO was controlled by a factor such as temperature. The region of strong anisotropy in the asthenospheric upper mantle evident along the N-S line (Fig. 6) corresponds roughly to the location of the Steens Mountain basalts (which are contemporaneous with the ~16 Myr old Columbia River basalts; see Long et al., 2009, and references therein) and the Holocene volcanic activity of Diamond Craters (Fig. 1). This possible spatial relationship is suggestive, but its nature remains obscure, given that our model has ruled out the possibility that anisotropy strength is controlled by variations in aligned partial melt in the shallowest upper mantle.

6.3. Pervasive anisotropy in the deep upper mantle beneath the Cascadia backarc

Our finding of strong anisotropy, and by inference strong olivine LPO, in the deep upper mantle (200-400 km depth) beneath the Cascadia backarc region has potentially important implications. Numerous studies on the rheology and deformation of the upper mantle (e.g., Karato and Wu, 1993; Karato et al., 2008) have suggested that olivine LPO is the primary mechanism for generating seismic anisotropy. However, there are indirect arguments, mainly based on previous observations of generally weaker anisotropy at depths greater than 200 km, that deformation in this depth range may be dominated by diffusion creep, rather than the dislocation

glide that is necessary to form LPO (e.g. Karato and Wu, 1993). Our finding of strong anisotropy in the deep upper mantle implies that there is, in fact, strong olivine LPO in this depth range, at least locally. This in turn suggests that the deep upper mantle is deforming in the dislocation glide regime, or, alternatively, that olivine LPO is being generated via a different mechanism at these depths. Miyazaki et al. (2013) recently proposed that diffusion creep may produce LPO in the upper mantle, although this idea remains controversial.

Recent results on deformation of olivine at relatively high pressure conditions may shed additional light on possible mechanisms for strong anisotropy in the deep upper mantle. Couvy et al. (2004) and Ohuchi and Irifune (2013) presented experimental evidence for the formation of olivine LPO at the pressures associated with the deep upper mantle; in particular, Ohuchi and Irifune (2013) argued for the development of A-type olivine fabric under water-rich conditions. More recently, Masuti et al. (2019) carried out deformation experiments on olivine single crystals and found evidence for the development of C-type olivine fabric under water-rich conditions, although their experiments were carried out at lower pressures than those of Ohuchi and Irifune (Ohuchi and Irifune (2013)). Given the geodynamic setting of our model in a subduction zone backarc, it is plausible that deformation is taking place under water-rich conditions, and we can envision a few possible scenarios that are consistent with our model. For the most part, the strong anisotropy in the deep upper mantle in our model is located above the slab surface (Fig. 4). If A-type olivine LPO dominates, as suggested by Ohuchi and Irifune (2013), then strong azimuthal anisotropy would suggest dominantly horizontal shearing (with a generally E-W shear direction). On the other hand, if C-type olivine LPO dominates, as suggested by Masuti et al. (2019), then a component of upwelling flow may align olivine C axes nearly vertically, producing strong azimuthal anisotropy. Geodynamic modeling results for the HLP region (Druken et al., 2011; Long et al., 2012) do suggest a component of upwelling associated with the rollback and steepening of the Cascadia slab, although significant horizontal flow is present as well.

6.4. Implications for reconciling surface wave and SKS constraints on anisotropy

An interesting aspect of our model is that it can be compared with models based on independent constraints, namely surface wave dispersion measurements. We are particularly interested in comparisons with the models of Yuan and Romanowicz (2010) and Lin et al. (2011) for the western U.S., because these models are based on joint inversion and/or interpretation of surface wave data and station-averaged SKS splitting measurements, and the surface wave model of Wagner and Long (2013), because that model was based on measurements made at HLP stations.

The model of Yuan and Romanowicz (2010) covers the entire western U.S. and has relatively coarse (~ 250 km) lateral resolution; we focus our comparison on the region beneath the HLP itself. This model features multiple layers of anisotropy beneath this region, with fast directions that vary from NE-SW fast directions in the shallow upper mantle (~ 70 - 100 km depth) to more nearly NW-SE fast directions in the mid-upper mantle (~ 200 - 250 km) to nearly E-W fast directions in the deepest upper mantle (~ 350 - 400 km). This model features relatively strong anisotropy in the deepest upper mantle, in that the anisotropy strength here is comparable to the anisotropy strength at shallower depths, but it is considerably weaker than in our preferred model (~ 2 - 3% vs. up to ~ 6 - 8%). This difference may reflect the fact that the model of Yuan and Romanowicz (2010) is based on a regularized inversion that may underestimate amplitudes, or it may be a consequence of their coarser lateral resolution. Interestingly, a comparison of mod-

els obtained by Yuan and Romanowicz (2010) (see their Fig. 7) that include only surface waveform constraints vs. those that include both surface waveforms and SKS splitting shows that when the SKS measurements are included, anisotropy in the deeper portions of the model (150 to 500 km depth) beneath the HLP is stronger and has a more nearly E-W fast direction. Furthermore, when a model is produced based only on surface waveforms, it strongly underpredicts the SKS splitting delay times. This is generally consistent with the inference from our study that the SKS observations themselves require a major contribution from anisotropy in the deep upper mantle. The agreement between our model and that of Yuan and Romanowicz (2010) is only partial, however, as our model does not include the considerable variability in fast axis orientations that is exhibited in the Yuan and Romanowicz (2010) model beneath the HLP.

The model of Lin et al. (2011), based on a combination of ambient noise and event-based surface waves, does not extend into the deep upper mantle, but at asthenospheric depths the model shows generally E-W fast directions, consistent with our model. At crustal depths (at which our model does not have resolution), the Lin et al. (2011) model shows relatively weak ($\sim 2\%$) and variable anisotropy. Lin et al. (2011) predicted SKS splitting fast directions and delay times based on their model; their predictions for the HLP region match the fast direction observations, but substantially underpredict the delay times (predicted times of up to ~ 1.2 s vs. observed times of up to ~ 2.5 s). Our finding of a substantial contribution to SKS splitting from anisotropy in the deep upper mantle is therefore consistent with the predictions of the Lin et al. (2011) model.

Our model provides an avenue for reconciling what had been thought of as apparently contradictory constraints on upper mantle anisotropy provided by surface wave and SKS splitting observations made at stations of the HLP experiment. Wagner and Long (2013) presented azimuthally anisotropic phase velocity maps based on surface wave dispersion measurements and a major focus of this paper was the apparently contradictory views of upper mantle anisotropy provided by the different types of data. The surface wave phase velocities, which have little or no sensitivity at depths greater than ~ 250 km, showed generally uniform fast orientations beneath the HLP with modest anisotropy strengths (values of up to $\sim 2.5\%$). Wagner and Long (2013) found that the anisotropy strengths suggested by the phase velocity maps were much smaller than needed to explain the SKS splitting delay times if all the anisotropy was distributed in the upper ~ 200 km of the mantle; furthermore, they argued that a strong contribution from crustal anisotropy (shallower than ~ 50 km) would have strongly affected the phase velocities at 33 and 40 s period, which was not observed. Wagner and Long (2013) left the resolution of this discrepancy to future work, and the model presented here now resolves the apparent paradox. Our preferred model for anisotropy beneath the HLP invokes strong anisotropy in the deep upper mantle, at a depth range that is beyond the sensitivity of the observations (at periods up to 143 s) used in the Wagner and Long (2013) surface wave model. The presence of deep upper mantle anisotropy can explain the apparent discrepancy between surface wave and SKS splitting constraints documented by Wagner and Long (2013).

7. Summary

We have presented a pseudo-3D model for the distribution of seismic anisotropy beneath the High Lava Plains of Oregon and its surrounding region in the backarc of the Cascadia subduction zone. This model was obtained in the framework of a probabilistic, finite-frequency SKS splitting intensity tomography approach applied to a data set of newly processed SKS splitting intensity measurements for stations of the HLP broadband array. The dense

station spacing of this array allowed us to resolve anisotropic structure, at length scales of ~ 50 km, in the depth range between 50–400 km. We found evidence for strong seismic anisotropy in the deep upper mantle beneath the Cascadia backarc, with generally weaker anisotropy in the 100–200 km depth range (with some local exceptions). There is little variability in the fast axis orientations, consistent with previous suggestions of a relatively simple mantle flow field. This finding is consistent with the idea of mantle flow beneath the Cascadia backarc that is driven by rollback subduction, as suggested by previous workers, and with the presence of lateral variations in olivine LPO strength within that simple flow field. Resolution tests demonstrate that our method is capable of resolving anisotropic structure throughout the model domain, and posterior probability distributions provide a sense for uncertainties in the model parameter estimations. Our finding of strong anisotropy in the deep upper mantle beneath the HLP helps to reconcile previously conflicting views of upper mantle anisotropy from surface wave constraints and SKS splitting data, and may suggest that deep upper mantle anisotropy is more important to the interpretation of shear wave splitting data sets than is often thought.

Declaration of competing interest

The authors declare that there is no conflict of interest regarding the publication of this article.

Acknowledgements

Seismic data from the High Lava Plains experiment (network code XC) and the EarthScope USArray Transportable array (network code TA) were accessed via the Data Management Center (DMC; <http://ds.iris.edu>) of the Incorporated Research Institutions for Seismology (IRIS). The facilities of the IRIS Consortium are supported by the National Science Foundation (NSF) under Cooperative Agreement EAR-1261681 and the DOE National Nuclear Security Administration. This work was supported by NSF grant EAR-1820815. We are grateful to Prof. Shun Karato for helpful discussions on olivine LPO and deep upper mantle anisotropy. We thank two anonymous reviewers whose constructive comments helped us to improve the presentation of the material.

Appendix A. Supplementary material

Supplementary material related to this article can be found online at <https://doi.org/10.1016/j.epsl.2020.116172>.

References

- Abt, D.L., Fischer, K.M., 2008. Resolving three-dimensional anisotropic structure with shear wave splitting tomography. *Geophys. J. Int.* 173 (3), 859–886.
- Bezada, M., Faccenda, M., Toomey, D., 2016. Representing anisotropic subduction zones with isotropic velocity models: a characterization of the problem and some steps on a possible path forward. *Geochem. Geophys. Geosyst.* 17 (8), 3164–3189. <https://doi.org/10.1002/2016GC006507>.
- Camp, V.E., 2019. Plume-modified mantle flow in the northern Basin and Range and southern Cascadia back-arc region since ca. 12 ma. *Geology* 47 (8), 695–699.
- Camp, V.E., Hanan, B.B., 2008. A plume-triggered delamination origin for the Columbia River basalt group. *Geosphere* 4 (3), 480–495.
- Camp, V.E., Ross, M.E., 2004. Mantle dynamics and genesis of mafic magmatism in the intermontane Pacific Northwest. *J. Geophys. Res., Solid Earth* 109 (B8). <https://doi.org/10.1029/2003JB002838>.
- Chen, C.-W., James, D.E., Fouch, M.J., Wagner, L.S., 2013. Lithospheric structure beneath the High Lava Plains, Oregon, imaged by scattered teleseismic waves. *Geochem. Geophys. Geosyst.* 14 (11), 4835–4848. <https://doi.org/10.1029/2010JB007795>.
- Chevrot, S., 2000. Multichannel analysis of shear wave splitting. *J. Geophys. Res., Solid Earth* 105 (B9), 21579–21590. <https://doi.org/10.1029/2000JB900199>.
- Chevrot, S., 2006. Finite-frequency vectorial tomography: a new method for high-resolution imaging of upper mantle anisotropy. *Geophys. J. Int.* 165 (2), 641–657.
- Couvy, H., Frost, D.J., Heidelbach, F., Nyilas, K., Ungár, T., Mackwell, S., Cordier, P., 2004. Shear deformation experiments of forsterite at 11 GPa–1400°C in the multianvil apparatus. *Eur. J. Mineral.* 16, 877–889.
- Druken, K., Long, M., Kincaid, C., 2011. Patterns in seismic anisotropy driven by rollback subduction beneath the High Lava Plains. *Geophys. Res. Lett.* 38 (13). <https://doi.org/10.1029/2011GL047541>.
- Eagar, K.C., Fouch, M.J., James, D.E., Carlson, R.W., 2011. Crustal structure beneath the High Lava Plains of eastern Oregon and surrounding regions from receiver function analysis. *J. Geophys. Res., Solid Earth* 116 (B2). <https://doi.org/10.1029/2010JB007795>.
- Favier, N., Chevrot, S., 2003. Sensitivity kernels for shear wave splitting in transverse isotropic media. *Geophys. J. Int.* 153 (1), 213–228.
- Ford, M.T., Grunder, A.L., Duncan, R.A., 2013. Bimodal volcanism of the High Lava Plains and northwestern basin and range of Oregon: distribution and tectonic implications of age-progressive rhyolites. *Geochem. Geophys. Geosyst.* 14 (8), 2836–2857. <https://doi.org/10.1002/ggge.20175>.
- Hales, T.C., Abt, D.L., Humphreys, E., Roering, J.J., 2005. A lithospheric instability origin for Columbia River flood basalts and Wallowa Mountains uplift in northeast Oregon. *Nature* 438 (7069), 842.
- Hawley, W.B., Allen, R.M., 2019. The fragmented death of the Farallon plate. *Geophys. Res. Lett.* 46 (13), 7386–7394. <https://doi.org/10.1029/2019GL083437>.
- Hayes, G.P., Moore, G.L., Portner, D.E., Hearne, M., Flamme, H., Furtney, M., Smoczyk, G.M., 2018. Slab2, a comprehensive subduction zone geometry model. *Science* 362 (6410), 58–61.
- Humphreys, E.D., Coblenz, D.D., 2007. North American dynamics and western US tectonics. *Rev. Geophys.* 45 (3). <https://doi.org/10.1029/2005RG000181>.
- James, D.E., Fouch, M.J., Carlson, R.W., Roth, J.B., 2011. Slab fragmentation, edge flow and the origin of the Yellowstone hotspot track. *Earth Planet. Sci. Lett.* 311 (1–2), 124–135.
- Jordan, B.T., Grunder, A.L., Duncan, R.A., Deino, A.L., 2004. Geochronology of age-progressive volcanism of the Oregon High Lava Plains: implications for the plume interpretation of Yellowstone. *J. Geophys. Res., Solid Earth* 109 (B10). <https://doi.org/10.1029/2003JB002776>.
- Karato, S.-i., Wu, P., 1993. Rheology of the upper mantle: a synthesis. *Science* 260 (5109), 771–778.
- Karato, S.-i., Jung, H., Katayama, I., Skemer, P., 2008. Geodynamic significance of seismic anisotropy of the upper mantle: new insights from laboratory studies. *Annu. Rev. Earth Planet. Sci.* 36, 59–95.
- Leonard, T., Liu, L., 2016. The role of a mantle plume in the formation of Yellowstone volcanism. *Geophys. Res. Lett.* 43 (3), 1132–1139.
- Lin, F.-C., Ritzwoller, M.H., Yang, Y., Moschetti, M.P., Fouch, M.J., 2011. Complex and variable crustal and uppermost mantle seismic anisotropy in the western United States. *Nat. Geosci.* 4 (1), 55. <https://doi.org/10.1038/ngeo1036>.
- Lin, Y.-P., Zhao, L., Hung, S.-H., 2014. Full-wave multiscale anisotropy tomography in southern California. *Geophys. Res. Lett.* 41 (24), 8809–8817. <https://doi.org/10.1002/2014GL061855>.
- Liu, K.H., Gao, S.S., 2011. Estimation of the depth of anisotropy using spatial coherency of shear-wave splitting parameters. *Bull. Seismol. Soc. Am.* 101 (5), 2153–2161. <https://doi.org/10.1785/0120100258>.
- Liu, K.H., Elsheikh, A., Lemnifi, A., Purevsuren, U., Ray, M., Refayee, H., Yang, B.B., Yu, Y., Gao, S.S., 2014. A uniform database of teleseismic shear wave splitting measurements for the western and central United States. *Geochem. Geophys. Geosyst.* 15 (5), 2075–2085. <https://doi.org/10.1002/2014GC005267>.
- Long, M.D., 2016. The Cascadia Paradox: mantle flow and slab fragmentation in the Cascadia subduction system. *J. Geodyn.* 102, 151–170.
- Long, M.D., Silver, P.G., 2009. Mantle flow in subduction systems: the slab flow field and implications for mantle dynamics. *J. Geophys. Res., Solid Earth* 114 (B10). <https://doi.org/10.1029/2008JB006200>.
- Long, M.D., De Hoop, M.V., Van Der Hilst, R.D., 2008. Wave-equation shear wave splitting tomography. *Geophys. J. Int.* 172 (1), 311–330.
- Long, M.D., Gao, H., Klaus, A., Wagner, L.S., Fouch, M.J., James, D.E., Humphreys, E., 2009. Shear wave splitting and the pattern of mantle flow beneath eastern Oregon. *Earth Planet. Sci. Lett.* 288 (3–4), 359–369.
- Long, M.D., Till, C.B., Druken, K.A., Carlson, R.W., Wagner, L.S., Fouch, M.J., James, D.E., Grove, T.L., Schmerr, N., Kincaid, C., 2012. Mantle dynamics beneath the Pacific Northwest and the generation of voluminous back-arc volcanism. *Geochem. Geophys. Geosyst.* 13 (8). <https://doi.org/10.1029/2012GC004189>.
- Masuti, S., Karato, S., Girard, J., Barbot, S.D., 2019. Anisotropic high-temperature creep in hydrous olivine single crystals and its geodynamic implications. *Phys. Earth Planet. Inter.* 290, 1–9.
- Miyazaki, T., Sueyoshi, K., Hiraga, T., 2013. Olivine crystals align during diffusion creep of Earth's upper mantle. *Nature* 502 (7471), 321.
- Mondal, P., Long, M.D., 2019. A model space search approach to finite-frequency SKS splitting intensity tomography in a reduced parameter space. *Geophys. J. Int.* 217 (1), 238–256.
- Monteiller, V., Chevrot, S., 2011. High-resolution imaging of the deep anisotropic structure of the San Andreas Fault system beneath southern California. *Geophys. J. Int.* 186 (2), 418–446.
- Ohuchi, T., Irfune, T., 2013. Development of A-type olivine fabric in water-rich deep upper mantle. *Earth Planet. Sci. Lett.* 362, 20–30.

- Reiss, M.C., Rumpker, G., 2017. Splitracer: Matlab code and GUI for semiautomated analysis and interpretation of teleseismic shear-wave splitting. *Seismol. Res. Lett.* 88 (2A), 392–409.
- Ruelle, D., 1999. *Statistical Mechanics: Rigorous Results*. World Scientific.
- Schmandt, B., Humphreys, E., 2010. Complex subduction and small-scale convection revealed by body-wave tomography of the western United States upper mantle. *Earth Planet. Sci. Lett.* 297 (3–4), 435–445.
- Sieminski, A., Paulssen, H., Trampert, J., Tromp, J., 2008. Finite-frequency SKS splitting: measurement and sensitivity kernels. *Bull. Seismol. Soc. Am.* 98 (4), 1797–1810.
- Silver, P.G., Savage, M.K., 1994. The interpretation of shear-wave splitting parameters in the presence of two anisotropic layers. *Geophys. J. Int.* 119 (3), 949–963.
- Smith, R.B., Jordan, M., Steinberger, B., Puskas, C.M., Farrell, J., Waite, G.P., Husen, S., Chang, W.-L., O'Connell, R., 2009. Geodynamics of the Yellowstone hotspot and mantle plume: seismic and GPS imaging, kinematics, and mantle flow. *J. Volcanol. Geotherm. Res.* 188 (1–3), 26–56.
- Tikoff, B., Benford, B., Giorgis, S., 2008. Lithospheric control on the initiation of the Yellowstone hotspot: chronic reactivation of lithospheric scars. *Int. Geol. Rev.* 50 (3), 305–324.
- Till, C.B., Grove, T.L., Carlson, R.W., Donnelly-Nolan, J.M., Fouch, M.J., Wagner, L.S., Hart, W.K., 2013. Depths and temperatures of <10.5 Ma mantle melting and the lithosphere-asthenosphere boundary below southern Oregon and northern California. *Geochem. Geophys. Geosyst.* 14 (4), 864–879. <https://doi.org/10.1002/ggge.20070>.
- Wagner, L.S., Long, M.D., 2013. Distinctive upper mantle anisotropy beneath the High Lava Plains and Eastern Snake River Plain, Pacific Northwest, USA. *Geochem. Geophys. Geosyst.* 14 (10), 4647–4666. <https://doi.org/10.1002/ggge.20275>.
- Wagner, L.S., Fouch, M.J., James, D.E., Hanson-Hedgecock, S., 2012. Crust and upper mantle structure beneath the Pacific Northwest from joint inversions of ambient noise and earthquake data. *Geochem. Geophys. Geosyst.* 13 (12). <https://doi.org/10.1029/2012GC004353>.
- Wagner, L.S., Fouch, M.J., James, D.E., Long, M.D., 2013. The role of hydrous phases in the formation of trench parallel anisotropy: evidence from Rayleigh waves in Cascadia. *Geophys. Res. Lett.* 40 (11), 2642–2646. <https://doi.org/10.1002/grl.50525>.
- Xue, M., Allen, R.M., 2006. Origin of the Newberry hotspot track: evidence from shear-wave splitting. *Earth Planet. Sci. Lett.* 244 (1–2), 315–322.
- Yuan, H., Romanowicz, B., 2010. Depth dependent azimuthal anisotropy in the western US upper mantle. *Earth Planet. Sci. Lett.* 300 (3–4), 385–394.
- Zhou, Q., Hu, J., Liu, L., Chaparro, T., Stegman, D.R., Faccenda, M., 2018. Western US seismic anisotropy revealing complex mantle dynamics. *Earth Planet. Sci. Lett.* 500, 156–167.